

Understanding the distribution of iron in multicrystalline silicon after emitter formation: Theoretical model and experiments

J. Schön,^{1,2,a)} H. Habenicht,¹ M. C. Schubert,¹ and W. Warta¹¹Fraunhofer Institute for Solar Energy Systems (ISE), Heidenhofstr. 2, 79110 Freiburg, Germany²University of Freiburg, Material Research Center, Stefan-Meier-Str. 21, 79104 Freiburg, Germany

(Received 3 September 2010; accepted 9 January 2011; published online 24 March 2011)

We studied the behavior of iron in multicrystalline silicon during phosphorus diffusion by spatially resolved measurements and physical modeling. We present improvements to the previously used models for internal gettering in multicrystalline silicon and phosphorus diffusion gettering. 2-dimensional simulations are used for optimization of the phosphorus diffusion processes for intentionally contaminated wafers regarding the iron distribution, without changing the emitter characteristics. Simulations and experimental results show a reduced interstitial iron concentration after an additional low temperature step at the end of the phosphorus diffusion. The concentration of iron precipitates was reduced by a short annealing at 900°C before the phosphorus diffusion, leading to a carrier lifetime three times higher than compared to the standard process. © 2011 American Institute of Physics. [doi:10.1063/1.3553858]

I. INTRODUCTION

The development of industrial solar cell concepts with high efficiency potential increases the demands on the quality of multicrystalline (mc) silicon. At the same time, selective and lowly doped emitters with lower gettering efficiencies have become more commonly used. Therefore a crucial factor is metal contaminations, which often limits the recombination lifetime in mc silicon. An effective gettering of the metals during solar cell processing could be an alternative to the cost-intensive purification of the feedstock materials. A concentration of metals in the emitter or in a few large precipitates¹ drastically reduces the recombination activity of the impurities. If the processes are optimized by enhanced temperature ramps to gain a higher carrier lifetime, the risk of shunting due to large metal precipitates² can not be disregarded. It has already been found that an extended low temperature gettering after solidification³ or at the end of the phosphorus diffusion process,⁴ reduces the interstitial iron (Fe_i) concentration and could increase the solar cell performance⁵ for highly contaminated silicon. Rinio *et al.*⁶ showed that the low temperature step is mainly effective at the edge of a mc ingot, where the metal contamination is high. We used simulations to find an optimized phosphorus gettering process for moderate iron concentrations and tried (experimentally) a pre-anneal at 900°C besides a post low temperature step. An emitter diffusion with an additional peak before the phosphorus diffusion aims for a reduction of the iron precipitate density. Plekhanov *et al.*⁷ suggested such a short pre-anneal for aluminum gettering from theoretical considerations. In this paper the results of theoretical and experimental investigations of the iron behavior during the phosphorus diffusion processes are presented. The comparisons of experimental and theoretical results test our iron models and improve the theoretical understanding.

II. MODEL FOR IRON IN MC SILICON

The differential equations for dissolved iron, iron precipitates, and phosphorus (for the phosphorus diffusion process) are solved, including their interaction terms. The main differences of the precipitation model used here which is based on the Fokker-Planck Equation,^{8,9} to the common model based on Ham's law,^{10,11} are: i) that the size distribution of the precipitates is modeled, giving more information and more accurate results in low supersaturated samples, and ii) that instead of the precipitate density itself, the density of sites at which a nucleation of precipitates is possible is used as an input parameter. This allows for the nucleation and complete dissolution of the precipitates during the simulation. The nucleation site density in mc silicon is assumed to be proportional to structural defects. Due to the high nucleation site density in mc silicon, precipitates grow only at a small portion of the nucleation sites. As was experimentally observed in Ref. 12 the resulting precipitation rates are not proportional to the density of structural defects and therefore are less sensitive to uncertainty in the input parameter, i.e., the proportionality factor between the nucleation site density and the density of structural defects. Additional trapping of iron at structural defects due to the local distortion of the lattice¹³ is considered by an additional term in the solubility. The predictive model for the phosphorus in-diffusion from a POCl₃ source distinguishes between the inactive concentration and the active phosphorus concentration, which is responsible for the higher solubility of iron in the emitter and determines the sheet resistance. The simultaneous interaction of iron with phosphorus in the emitter and with the unevenly distributed structural defects via precipitates is taken into account by using a two dimensional structure.

A. Trapping of iron at extended defects

Multicrystalline (mc) silicon is an inhomogeneous material with dislocation densities ranging from 10² cm⁻² in good grains to more than 10⁷ cm⁻² in dislocation clusters

^{a)}Author to whom correspondence should be addressed. Electronic mail: jonas.schoen@ise.fraunhofer.de.

and grain sizes varying from microns to several centimeters. Mobile impurities are trapped at these extended defects by two mechanisms: i) precipitation of supersaturated impurities, and ii) segregation due to higher solubility in the strain field. Iron concentrations 3 orders of magnitude higher than in undisturbed areas can be found in the vicinity of the defects.¹⁴

In the case of mc silicon the density of possible precipitation sites is the product of the dislocation density and the linear density of precipitation sites along a dislocation. The linear density of precipitation sites was chosen to be $l_p = 3.3 \times 10^5 \text{ cm}^{-1}$. For simplification, grain boundaries are interpreted as lines of dislocations. It is important to note that although the density of possible precipitation is proportional to the structural defects the density of precipitates is not.

Increased equilibrium iron solubility due to local distortion of the lattice in the vicinity of extended defects (SD) is considered by adding an additional term to the iron solubility C_{Sol} :

$$C_{Sol}(\text{SD}) = C_{Sol}(\text{mono})(1 + C_1 \times \text{SD}), \quad (1)$$

$$C_1 = 0.5\pi r_{SD}^2 \exp(E_i/k_B T).$$

We decided to modify our first approach¹⁵ for the segregation to extended defects and reduce the influence of structural defects on the solubility at high temperature, which is not consistent with theoretical analyses of the interaction of metals and dislocations.¹⁶ The area of the strain in which the iron is preferentially located is experimentally difficult to measure and estimated with the radius $r_{SD} = 15 \text{ nm}$. In this area the interaction energy between dislocations and iron point defects E_i is inhomogeneous, reaching more than 1 eV in a small core region and less than 0.8 eV in the vicinity of the dislocation.^{16,17} The factor 0.5 in C_1 is derived from the side with negative E_i . We use an interaction energy between dislocations and iron point defects E_i of 0.6 eV.

The solubility in the vicinity of extended defects used in this model influences the iron distribution only at lower temperatures and has almost no influence at temperatures above 800°C. Due to the higher proportion of large grains on the overall wafer, the higher solubility in the vicinity of extended defects often has only a minor effect on the mean Fe_i concentrations. In most cases a precipitation model alone should be able to explain mean values as was found in Ref. 18.

B. Phosphorus diffusion gettering of iron in mc silicon

Based on the standard diffusion models from the Sentaurus Process[®] platform,¹⁹ the diffusion parameters and the boundary conditions for phosphorus are improved.²⁰ During the POCl_3 flux the phosphorus concentration at the surface of the phosphorus silicate glass (PSG) remained constant, while segregation of the phosphorus at the silicon PSG interface is simulated, taking the PSG growth into account.

The redistribution of iron during phosphorus diffusion is modeled with a segregation mechanism, caused by the high active phosphorus concentration in the emitter. A higher sol-

ubility of iron in the emitter is modeled by assuming double negatively charged substitutional iron and a pairing of this substitutional iron with positively charged phosphorus. A substitutional state can be expected from a first principle analysis²¹ and a double negatively charged state in combination with a phosphorus pairing from solubility measurements.²² The solubility of the neutral iron is independent from the net doping in silicon, whereas the equilibrium concentration of negatively charged states and pairs increases in the emitter with the concentration of active phosphorus. We use the same effective segregation coefficient $k_{\text{Fe}}(\text{P}^+)$ between emitter and base as in Refs. 20 and 23:

$$k_{\text{Fe}}(\text{P}^+) = 1 + 1.5 \times 10^{-27} \times \exp\left(\frac{1.359}{kT}\right) \times \left(\frac{n}{n_i}\right)^2 \times \text{P}^+, \quad (2)$$

with the parameters achieved from the experimental data. The additional term in the segregation coefficient proportional to the active phosphorus concentration and the square of the electron concentration n is the contribution of the iron phosphorus pairs to the solubility. Gilles *et al.*²² found a decreased diffusivity of iron in highly phosphorus doped silicon. Therefore substitutional iron and iron-phosphorus pairs are assumed to be immobile and only interstitial iron contributes to the diffusivity.

III. EXPERIMENT

Parallel wafers from the middle and top regions of a block intentionally contaminated with 20 ppma iron in the melt and a reference block are used for the experimental study of internal and external gettering. The 190 μm thick p-doped wafers were chemically polished in order to remove the saw damage and flatten the surface. They were divided into groups: as-cut, phosphorus diffusion (PD) 1–3, and oxidation. For each process variation three $5 \times 5 \text{ cm}^2$ wafers are processed. Three different temperature profiles were used in the phosphorus diffusion processes (Fig. 1): a standard process (PD 1), a process with a slow cooling ramp and one hour at 550°C after the phosphorus diffusion (PD 2), and a process with a 900°C peak before the phosphorus diffusion (PD 3). After the emitter formation in a tube furnace with the POCl_3 source, the wafers were cooled in air to room temperature. For a better comparison, the sheet resistances should be the same after the three phosphorus diffusions. After stages PD 1 and PD 3, a sheet resistance of 90 Ω/sq (a possible industrial standard in the near future), was measured on both sides of FZ reference wafers. Due to the lower solubility of phosphorus at 550°C and the resulting deactivation, the sheet resistance after PD 2 is 20% higher (in the experiment and the simulation). Afterward, the PSG layers as well as 5 μm silicon (including the emitter) at both sides of the wafer are removed and silicon nitride layers are deposited at 350°C for surface passivation. Oxidation processes with equal temperature profiles enable us to distinguish between the redistribution of iron due to the high temperature and due to phosphorus diffusion gettering.

Spatially resolved lifetime measurements captured by quasi-steady-state photoconductance calibrated photoluminescence imaging were performed. One measurement was

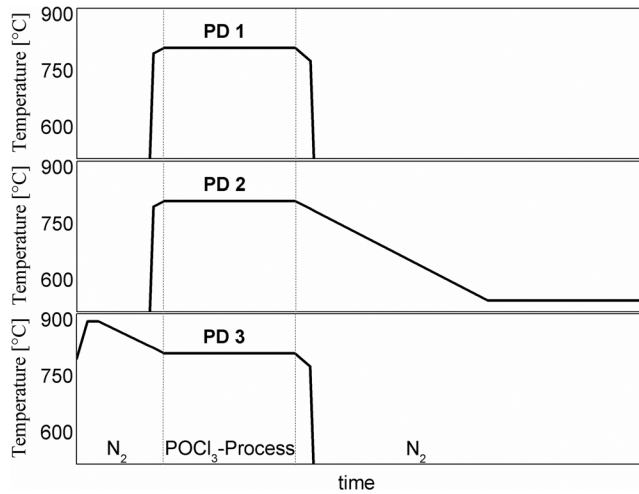


FIG. 1. Temperature profiles of the standard phosphorus diffusion (PD 1) and the variations PD 2 and PD 3.

obtained after keeping the wafer in the dark where FeB pairs were formed, and the other measurement was obtained after the splitting of the FeB pairs. FeB pairs have been broken by 2 min laser illumination (790 nm, photon density $6.375 \times 10^{17} \text{ cm}^{-2} \text{ s}^{-1}$). From the two measurements and the different Shockley-Read-Hall (SRH) lifetime dependencies of Fe_i and FeB pairs, an image of the interstitial iron concentration can be calculated.²⁴ With a Si-CCD camera a resolution of $50 \times 50 \mu\text{m}^2$ for the $50 \times 50 \text{ mm}^2$ wafers are achieved. Wafers are excited by a 790 nm laser with a photon density of $8.67 \times 10^{16} \text{ cm}^{-2} \text{ s}^{-1}$ (equivalent to 0.34 suns), generating carriers near the front surface. The low laser intensity ensures that only an insignificant fraction of the FeB pairs break during the 0.5 s of lifetime measurement. In samples with low carrier lifetime the FeB pairs split more slowly under illumination (see Ref. 25 for a discussion). This allows us to use integration times up to 3 s for as-cut samples in order to reduce noise. For the reference samples with a high lifetime the excess carrier density is nearly homogeneous over the whole sample thickness, due to the electron diffusion. For as-cut samples, the underestimation of the Fe_i concentration due to the inhomogeneous carrier depth profiles is corrected as proposed in Ref. 26. The interstitial iron concentrations are calculated, using the parameters from Istratov *et al.*²⁷ for Fe_i and from Macdonald *et al.*²⁸ for FeB.

IV. RESULTS

The phosphorus diffusion gettering model for iron as well as the process variations have been tested at: i) reference wafers with a low total iron concentration which is considerably reduced during phosphorus diffusion, ii) wafers with a medium total iron concentration which is slightly reduced during phosphorus diffusion, and iii) wafers with a high total iron concentration which stays almost constant during phosphorus diffusion. The simulated Fe_i concentrations in a model structure with areas of different crystal quality are compared with measured Fe_i concentrations. However, first the results without an external gettering sink are presented.

A. Internal gettering for wafers with an iron concentration of $3.5 \times 10^{13} \text{ cm}^{-3}$

The phosphorus diffusion and the iron gettering are simulated for a 2-dimensional cross section of a wafer through a grain boundary, a grain 3 mm in width and $210 \mu\text{m}$ at a highly dislocated area [see Fig. 2(a)]. The simulations of the precipitation during the cooling process of the block start directly after solidification, using the iron concentration measured by neutron activating analyses (NAA)²⁹ and the temperature profiles of the crystallization process. The simulated Fe_i concentrations for wafers in the as-cut state with a total iron concentration of $3.5 \times 10^{13} \text{ cm}^{-3}$ are shown in Figs. 2(b) and 2(c). The simulated mean Fe_i concentration of $3.5 \times 10^{12} \text{ cm}^{-3}$ is consistent with the measured $2.1 \times 10^{12} \text{ cm}^{-3}$ ([see Fig. 3(a)]). The precipitation sites are located along the dislocation and therefore not evenly distributed in the grains. The simulated Fe_i concentration varies around the dislocations in the grain. A similar effect is not expected in the measurements, due to the pixel size of $50 \times 50 \mu\text{m}^2$ and the carrier diffusion length of 50–500 μm . If we consider blurring due to carrier diffusion in our simulation and average over 50 μm , the variation around a dislocation is less than 5%, which is in the range of background noise. The simulated Fe_i concentration in the grain is around six times higher than in the vicinity of the grain boundary and eight times higher than in the vicinity of the dislocation cluster, which is in good agreement with the measurement. Comparing the measured and simulated Fe_i concentration, one has to keep in mind the carrier diffusion during the measurements, which is responsible for smearing around structural defects and explains the smaller contrast in the Fe_i images. The denuded zones appearing in the Fe_i images can be found with the same widths in the simulated results.

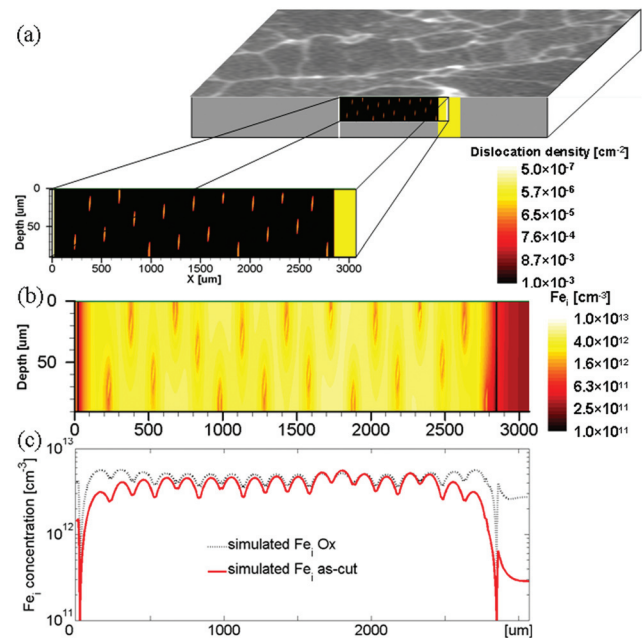


FIG. 2. (Color online) The Fe_i concentration is simulated (b) for a cross section through three areas with different precipitation site density, shown in (a). (c) Depth-averaged Fe_i concentration in the as-cut state and after oxidation.

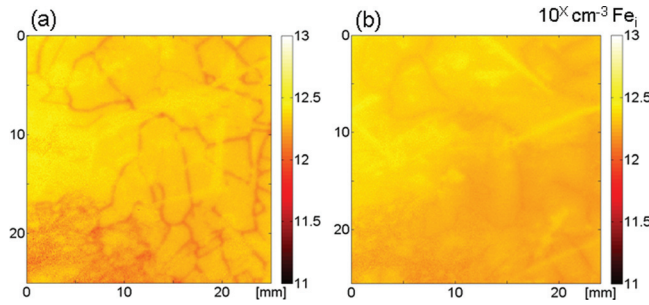


FIG. 3. (Color online) Measured Fe_i concentration in (a) the as-cut state and (b) after oxidation. The mean Fe_i concentration in both cases is $2 \times 10^{12} \text{ cm}^{-3}$, but after oxidation the Fe_i concentration in the vicinity of structural defects is higher and the denuded zones are smaller.

The simulated as-cut state is used as an input file for the simulation of further processing steps. After an oxidation with the standard temperature profile a mean Fe_i concentration of $2 \times 10^{12} \text{ cm}^{-3}$ is measured [see Fig. 3(b)], whereas $4.4 \times 10^{12} \text{ cm}^{-3}$ was expected from the simulation [Fig. 2(b)]. In the simulation as well as in the measured Fe_i images, the contrast between the grain and the grain boundary becomes smaller after oxidation. The denuded zones get thinner, due to out-diffusion from the grain boundaries^{30,31} and less iron is precipitated during the fast cooling.

B. Emitter process variation for wafers with an iron concentration of $3.5 \times 10^{13} \text{ cm}^{-3}$

The simulated Fe_i concentrations after the three phosphorus diffusions are shown in Fig. 4 together with the Fe_i image after PD 3. After the standard phosphorus diffusion the Fe_i concentration is reduced by 1 order of magnitude within the grains, but remains almost constant at the dislocation cluster and the grain boundary, due to dissolution of the precipitates. The additional peak (PD 3) has only a small influence on the concentration of dissolved iron, whereas the additional plateau at 550°C (PD 2) is quite effective. The reasons for this are: i) the higher segregation coefficient [Eq. (2)] between emitter and base, leading to an enhanced external gettering, and ii) precipitation of highly supersaturated iron during the long low temperature step. The simulated total iron concentration after phosphorus diffusion is reduced by a factor of 4 and is almost the same for the three variations. Table I summarizes the measured mean carrier lifetimes in the as-cut state and after different processing steps (see Fig. 1) for the wafers with an initial iron concentration of $3.5 \times 10^{13} \text{ cm}^{-3}$ and the reference wafers. As in earlier experiments,^{32,33} it was observed that the carrier lifetime in good grains can be easily improved by a phosphorus diffusion, whereas the changes in areas with high crystal defect density are small. By far, the highest mean carrier lifetime was measured after PD 3, whereas an additional 550°C temperature treatment has no positive influence. It should be noted that the additional peak before the phosphorus diffusion also improves the carrier lifetime in areas with high crystal defect density.

The measured Fe_i concentration after phosphorus diffusion with a preceding temperature peak (PD 3) is shown in Fig. 4(c) and has a mean value of $4.1 \times 10^{10} \text{ cm}^{-3}$. After PD 1,

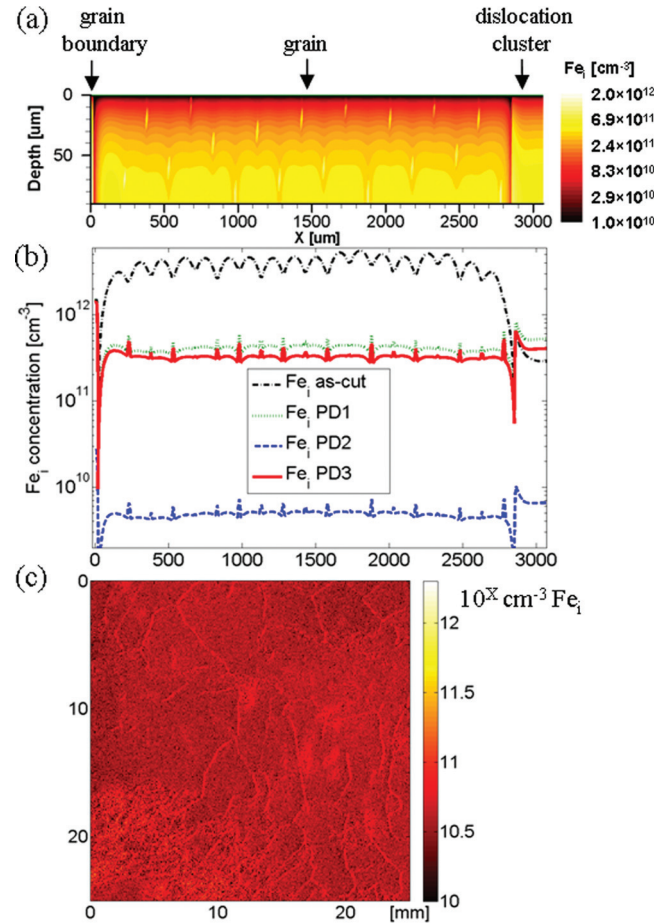


FIG. 4. (Color online) (a) Simulated Fe_i concentration after PD 3 for the cross section shown in Fig. 2(a). The Fe_i concentration in the bulk decreases toward the surface in the simulation, due to the gettering effect of the emitter. (b) The simulated Fe_i concentrations (depth-averaged) after the three process variations compared to the as-cut state. The Fe_i concentration in the vicinity of the grain boundary and the vicinity of the dislocation cluster is higher than within the grain, but the contrast is rather small for the three process variations. (c) Measured Fe_i concentration after phosphorus diffusion with an additional peak (PD 3). A higher Fe_i concentration was measured at pixels with grain boundaries and at dislocation clusters, e.g., in the lower left side of (c).

a mean Fe_i concentration of around $7 \times 10^{10} \text{ cm}^{-3}$ was measured, which is slightly above the detection limit of around $4 \times 10^{10} \text{ cm}^{-3}$ for a carrier lifetime of $7 \mu\text{s}$, leading to noisy Fe_i images. The Fe_i concentration after PD 2 is already below the detection limit. The contrast between areas of different crystal quality is quite small, but the Fe_i concentrations in the simulations and the Fe_i images are higher at grain boundaries and dislocation clusters compared to the as-cut wafers.

TABLE I. Measured carrier lifetime at parallel wafers (Fe_i state/excess carrier density $\Delta n = 10^{14} \text{ cm}^{-3}$).

| Wafer type | As-cut(μs) | PD 1 (μs) | PD 2 (μs) | PD 3 (μs) | Ox (μs) |
|---|-------------------------|------------------------|------------------------|------------------------|----------------------|
| Fe = $3.5 \times 10^{13} \text{ cm}^{-3}$ | 1.3 | 7 | 5.5 | 22 | 1.5 |
| Reference | 23 | 32 | 34 | 34 | 22 |
| Reference near top | 6.5 | 43 | — | — | 4.8 |

Figure 5 summarizes the simulated and measured results for the wafers with an iron contamination of $3.5 \times 10^{13} \text{ cm}^{-3}$. The simulated Fe_i concentration is higher than the Fe_i imaging of the wafers after phosphorus diffusion with a preceding temperature peak (PD 3) (see Fig. 4) and standard phosphorus diffusion (PD 1). The deviation of the Fe_i concentration could be due to uncertainties in the input parameters in the simulations, i.e., total iron concentrations that are too high, incorrect temperature ramps, and a segregation coefficient that is too low in the model, or additional gettering effects. Systematic errors in Fe_i imaging must also be taken into account. The Fe_i concentration in the bulk decreases toward the surface in the simulation, due to the gettering effect of the emitter (see Fig. 4). This depth dependence Fe_i concentration and the low lifetime lead to an underestimation of the Fe_i concentration up to a factor of 2 in the measurements. Considering the number of uncertainties in the experiment and the simulations the correlation is satisfying.

C. Reference wafers

For the as-cut wafers from the reference ingot, a mean Fe_i concentration of $1.6 \times 10^{11} \text{ cm}^{-3}$ and $6.8 \times 10^{11} \text{ cm}^{-3}$ were measured. The total iron concentration was below the NAA detection limit of $7.2 \times 10^{12} \text{ cm}^{-3}$. The Fe_i concentration slightly increases after oxidation, but is still smaller than the solubility during oxidation and the concentration in the contaminated wafers. This allows the assumption that the iron in the reference wafers is completely dissolved during oxidation. In the contaminated samples the Fe_i concentration after the oxidation is nearly 50% of the solubility at the oxidation temperature. Due to the smaller precipitation rates during the cooling process in the lower contaminated samples and the small differences between the Fe_i concentrations before and after oxidation, more than 50% of the iron is in the interstitial state or paired with boron atoms after oxidation and is already in the as-cut state. After the three

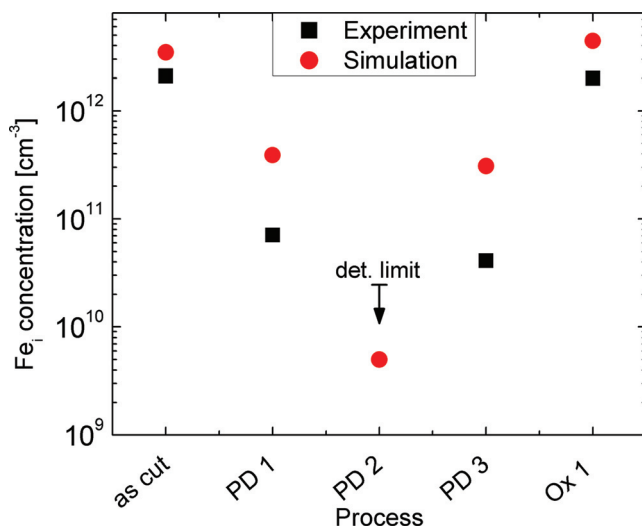


FIG. 5. (Color online) Comparison of simulated and measured mean Fe_i concentration in the as-cut state and after different processing steps (see Fig. 1).

phosphorus diffusion processes, the Fe_i concentrations are below the detection limit and the carrier lifetimes are at the same level (see Table I).

D. Emitter process variation for wafers with an iron concentration of $1 \times 10^{16} \text{ cm}^{-3}$

For the wafers from the top of the contaminated ingot, a total iron concentration of $1 \times 10^{16} \text{ cm}^{-3}$ was measured with NAA. The Fe_i images before and after the standard phosphorus diffusion along with the corresponding simulations are shown in Fig. 6. Table II summarizes the measured carrier lifetimes and mean Fe_i concentrations in areas of different crystal quality. Areas with high dislocation density and grain boundaries have lower Fe_i concentration and higher lifetime before phosphorus diffusion. In the area with large grains the Fe_i concentration and the carrier lifetime is as high as in the wafers contaminated with $3.5 \times 10^{13} \text{ cm}^{-3}$. The wafers from the top region have a higher proportion of areas with high crystal defect density than the wafers from medium ingot height, resulting in an overestimation of the mean Fe_i concentration in the simulation. A mean Fe_i concentration of $3.3 \times 10^{12} \text{ cm}^{-3}$ was simulated for the as-cut state, whereas $1.5 \times 10^{12} \text{ cm}^{-3}$ was measured for the wafer shown in Fig. 6(a). Again, the contrast between the grain and areas with high density of structural defects in the simulation is in consistency with the measurement [see Figs. 6(a) and 6(c)].

After PD 1, the iron concentration is reduced and the carrier lifetime is increased from $0.8 \mu\text{s}$ to $9.8 \mu\text{s}$ in the large grains [rectangle in upper left part of Fig. 6(a)], indicating that the dissolved iron was limiting the carrier lifetime

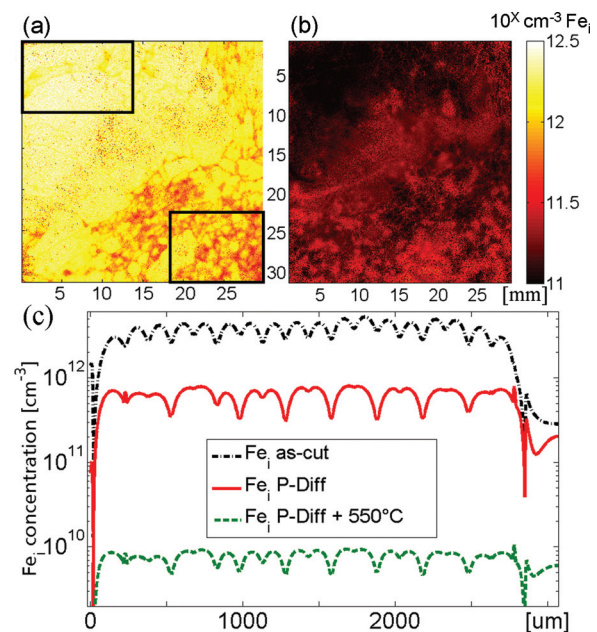


FIG. 6. (Color online) Measured Fe_i concentration (a) before and (b) after phosphorus diffusion in comparison with the simulations (linescan) (c) for an initial iron concentration of $1 \times 10^{16} \text{ cm}^{-3}$. After phosphorus diffusion with an additional low temperature step the measured Fe_i concentration is below the detection limit, therefore only the simulation is shown. The rectangles in the upper left part and in the lower right part of (a) are used to represent areas with high and low crystal quality.

TABLE II. Measured carrier lifetimes τ (Fe_i state/excess carrier density $\Delta n = 10^{14} \text{ cm}^{-3}$) and mean Fe_i concentrations in the marked areas of Fig. 6.

| | As-cut | | Standard PD | | PD + 550°C step | |
|----------------------|--------------------------|--|--------------------------|--|--------------------------|--|
| Crystal quality | τ [μs] | Fe_i conc. [cm^{-3}] | τ [μs] | Fe_i conc. [cm^{-3}] | τ [μs] | Fe_i conc. [cm^{-3}] |
| High [see Fig. 6(a)] | 0.8 | 2.2×10^{12} | 9.8 | 1.0×10^{11} | 11 | $< 2 \times 10^{10}$ |
| Low [see Fig. 6(a)] | 1.6 | 9.3×10^{11} | 4.8 | 2.8×10^{11} | 5.0 | $< 1 \times 10^{11}$ |

before the phosphorus diffusion. A further reduction of the Fe_i concentration below the detection limit by an additional 550°C anneal improves the carrier lifetime slightly to 11 μs which is comparable with good grains in medium contaminated wafers. In areas with a high density of crystal defects [rectangle in the lower right part of Fig. 6(a)], the reduction of the Fe_i concentration to $2.8 \times 10^{11} \text{ cm}^{-3}$ (PD 1) increases the carrier lifetime by a factor of three. An additional low temperature ramp (PD 2) reduces the Fe_i concentration below the detection limit and increases the carrier lifetime in large grains.

After phosphorus diffusion the simulated Fe_i concentration in areas with high dislocation density is around $1.7 \times 10^{11} \text{ cm}^{-3}$ and almost equal to the measured concentration, whereas the Fe_i concentration in the grain is higher than in the measurements. This leads to higher values in the grain than in areas with a high density of structural defects, although the contrast between areas of different crystal quality is lower than in the as-cut state. The simulation for a further low temperature step shows an almost homogenous Fe_i concentration of $9 \times 10^9 \text{ cm}^{-3}$.

V. DISCUSSION

A. Interstitial and total iron concentration

The simulated and measured mean Fe_i concentrations as well as the simulated total iron concentrations after PD 1 for various initial iron concentrations are summarized in Fig. 7. Phosphorus diffusion reduces the total and Fe_i concentration

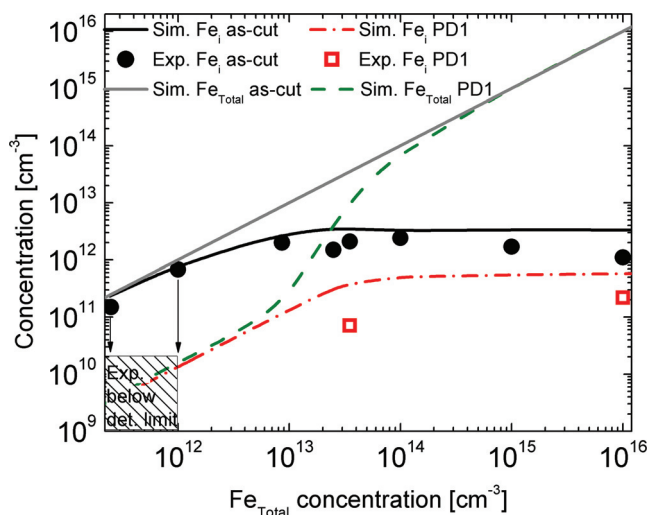


FIG. 7. (Color online) Comparison of simulated and measured mean Fe_i concentration in the as-cut state and after standard phosphorus diffusion for various total iron concentrations.

by 2 orders of magnitude up to an initial iron concentration of $1 \times 10^{13} \text{ cm}^{-3}$. Above an initial iron concentration of $5 \times 10^{13} \text{ cm}^{-3}$ only the mean Fe_i concentration is significantly reduced.

Although the differences in the Fe_i concentrations of a series of measurements are reliable, the use of different SRH-parameters for calculating the Fe_i concentrations from the carrier lifetimes in the two states could result in an overall shift of the Fe_i concentrations. The published SRH-parameters for Fe_i and FeB reveal considerable as shown in differences.²⁸ Thus the consistency of the shapes of the measured and simulated curves is more important than an exact match of the values. The Fe_i concentration in the as-cut state increases rapidly for low initial iron concentrations and has a maximum determined by the cooling ramp after crystallization, whereas the proportion of precipitated iron increases rapidly for iron concentrations above $1 \times 10^{12} \text{ cm}^{-3}$. The differences in the crystal defect density of the measured samples are not considered in the simulated mean values in Fig. 7, leading to larger deviations especially for the highly contaminated top wafers (see Table II). As in the simulations the measured Fe_i concentrations after phosphorus diffusion also increase for an increasing initial iron concentration for high initial concentrations. However the number of measured points is too small to confirm the two different regimes of the simulated curve, i.e., the slower rise for high initial iron concentrations is not discernible.

Kvande *et al.*³⁴ and Coletti *et al.*³⁵ found higher Fe_i concentrations after crystallization and phosphorus diffusion in experiments with intentionally contaminated mc silicon. The qualitative shape of the measured curves are comparable with our simulations, although an emitter with lower sheet resistance and probably different temperature ramps after solidification were used.

B. Carrier lifetime and precipitates

The Shockley-Read-Hall lifetime for an Fe_i concentration of $7 \times 10^{10} \text{ cm}^{-3}$ is 80 μs , indicating that Fe_i is not responsible for the differences in the carrier lifetimes between the iron contaminated wafers (7 μs) and reference wafers (32 μs) after standard phosphorus diffusion. Consequently a further reduction of the Fe_i concentration (PD 2) increases the carrier lifetime only for the highly contaminated wafers from the top of the ingot. If the iron point defects are not responsible for the reduced carrier lifetimes after phosphorus diffusion, the latter could be due to crystal defects caused by the higher metal concentration or other iron defects, which could be, in principle, getterred. The large increase in the carrier lifetime after PD 3 (with 900°C peak) is evidence that iron precipitates are detrimental after phosphorus diffusion.

For this reason we look more closely at the simulated concentrations of precipitates after the different high temperature steps and the recombination activity without Fe_i and FeB recombination (Fig. 8). The recombination activity without recombination due to Fe_i point defects can be extracted from the measured lifetime of parallel wafers:

$$R_{\text{woFei}} = \frac{1}{\tau_{\text{other}}} = \frac{1}{\tau_{\text{measured}}} - \frac{1}{\tau_{\text{Fei}}}. \quad (3)$$

The precipitates have been sorted into three classes (small, medium, and large) in order to show the redistribution of iron atoms during the high temperature process steps.

Without phosphorus gettering, a small shift toward larger precipitates for oxidized wafers show dissolution of small precipitates during the high temperature step and a ripening of large precipitates. An additional external gettering reduces the total iron concentration and thus the number of precipitates. The equilibrium concentration of iron around large precipitates at 900°C is $4 \times 10^{13} \text{ cm}^{-3}$ (Ref. 36), leading to a complete dissolution of small and medium sized iron precipitates and a shrinking of larger precipitates during the short 900°C peak. Coming from higher temperatures (PD 3), the concentration of mobile iron atoms is higher at the start of the phosphorus diffusion and iron can be quickly and effectively gettered. Another advantage of the temperature peak can be seen in Fig. 8. Compared to the cooling process after solidification, the supersaturation after the 900°C peak is much lower, leading to a growth of the existing large precipitates with almost no nucleation of new precipitates. Therefore the densities of small and especially medium sized iron precipitates are lower after the process with the 900°C peak. Small precipitates nucleate only at the temperature ramp to room temperature and the subsequent SiN_x deposition process. The recombination activity of the precipitates depends on the size of the precipitates,³⁷ thus small precipitates have only a minor effect on the carrier lifetime. Buonassisi *et al.*¹ showed that a concentration of iron in a few large precipitates results in higher carrier lifetimes. The

same trend could be observed in the sum of medium and large precipitates and the recombination activity without Fe_i and FeB recombination, allowing for the assumption that the reduction of precipitates is responsible for the higher lifetimes after phosphorus diffusion with an additional temperature peak. One has to keep in mind that a linear dependency between precipitation density and recombination activity cannot be expected, due to the extremely inhomogeneous distribution of the dislocations and precipitates. The additional 900°C peak halves the number of precipitates, but their concentration is high enough to explain the differences in carrier lifetime between the contaminated wafers and the reference wafers. The pre-anneal would have almost no influence on the simulation results, using a model with a mean radius for all precipitates.

The redistribution of the impurities due to the additional 900°C peak and the resulting gain in lifetime depends strongly on the level and the solubility of the impurities. Using higher peak temperatures with rates of solubility well above the iron concentration could result in high Fe_i concentrations, if the precipitate density is too low to trap the remaining Fe_i atoms after phosphorus diffusion.

VI. CONCLUSIONS

A 2-dimensional model for precipitation and phosphorus diffusion gettering of iron in multicrystalline silicon is proposed, which explains the experimental results for emitter process variations. The simulations have been realized for different iron contamination levels and are consistent with the spatially resolved Fe_i measurements and carrier lifetimes at all process stages. The dissolved iron around dislocations and grain boundaries in higher contaminated as-cut samples is captured by precipitates, leading to lower concentrations of dissolved iron at the structural defects as shown in the simulations and the experiments. We observe and explain the strong reduction of the Fe_i concentration within the grains and minor changes in areas with high defect densities during standard phosphorus diffusion.

Iron point defects, which are detrimental in the as-cut state, are reduced by more than 1 order of magnitude during standard phosphorus diffusion and can further be reduced to concentrations below 10^{10} cm^{-3} with a 90 min low temperature anneal at 550°C . Strong indications were found that iron precipitates and not interstitial iron are limiting the carrier lifetime after phosphorus diffusion in the contaminated wafers. We propose a short temperature peak directly before the phosphorus diffusion in order to significantly improve the gettering effect. We experimentally observed an increase in the carrier lifetime for wafers contaminated with $3.5 \times 10^{13} \text{ cm}^{-3}$ iron after emitter diffusion by a factor of 3. Our simulations indicate that the large increase in lifetime is due to a reduced density of small and medium precipitates. The additional temperature peak before the phosphorus diffusion improves the carrier lifetime not only inside large grains but also in areas with high crystal defect density. We expect that a 900°C pre-annealing is not always ideal and the optimal peak temperature depends on the level of impurities.

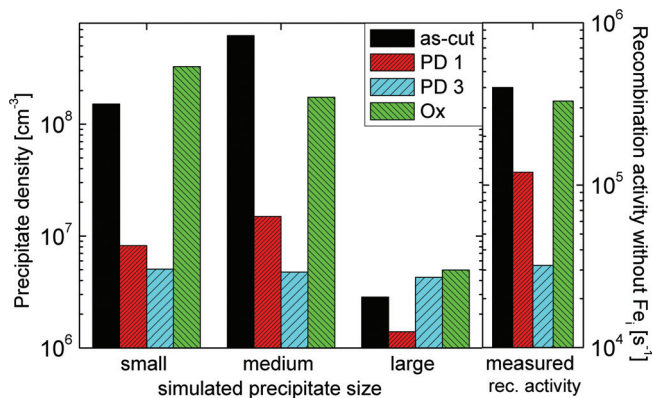


FIG. 8. (Color online) Simulated densities of small, medium, and large precipitates before and after different processing steps (see Fig. 1). Iron precipitates are divided in three groups: Fe atoms per precipitate <1000 (small), $1000 < \text{Fe atoms} < 5 \times 10^5$ (medium), and $\text{Fe atoms} > 5 \times 10^5$ (large). The measured recombination activities without recombination due to Fe_i after the four processing steps are shown at the right side (right y-axis)

ACKNOWLEDGMENTS

This work was funded by the German Ministry for the Environment, Nature Conservation and Nuclear Safety under Contract no. 0 327 650E (SolarFocus) and internally funded by the Fraunhofer Society by the project Silicon Beacon. The authors would like to thank H. Behnken from Access e.V. for the temperature profiles, A. Haarahiltunen for the fruitful discussions, C. Majenz for the support during the measurement procedure, and J. Costello for proofreading the article.

- ¹T. Buonassisi, A. A. Istratov, M. A. Marcus, B. Lai, Z. Cai, S. M. Heald, and E. R. Weber, *Nature Mater. Lett.* **4**, 676 (2005).
- ²T. Buonassisi, O. F. Vyvenko, A. A. Istratov, E. R. Weber, G. Hahn, D. Sontag, J. P. Rakotoniaina, O. Breitenstein, J. Isenberg, and R. Schindler, *J. Appl. Phys.* **95**, 1556 (2004).
- ³R. Krain, S. Herlufsen, and J. Schmidt, *Appl. Phys. Lett.* **93**, 152108 (2008).
- ⁴M. B. Shabani, T. Yamashita, and E. Morita, *Solid State Phenom.* **131–133**, 399 (2008).
- ⁵M. D. Pickett and T. Buonassisi, *Appl. Phys. Lett.* **92**, 122103 (2008).
- ⁶M. Rinio, A. Yodyunyong, M. Pirker, C. Zhang, D. Günther, P. Botchak, S. Keipert, D. Borchert, M. Heuer, and A. Montesdeoca-Santana, in *Proceedings of the 24th European Photovoltaic Solar Energy Conference* (WIP, Hamburg, Germany, 2009) p. 1816–9.
- ⁷P. S. Plekhanov, R. Gafiteanu, U. M. Gösele, and T. Y. Tan, *J. Appl. Phys.* **86**, 2453 (1999).
- ⁸A. Haarahiltunen, H. Väinölä, O. Anttila, M. Yli-Koski, and J. Sinkkonen, *J. Appl. Phys.* **101**, 043507 (2007).
- ⁹A. Haarahiltunen, H. Savin, M. Yli-Koski, H. Talvitie, M. I. Asghar, and J. Sinkkonen, *Mater. Sci. Eng., B* **159–160**, 248 (2009).
- ¹⁰H. Hieslmair, A. A. Istratov, T. Heiser, and E. R. Weber, *J. Appl. Phys.* **84**, 713 (1998).
- ¹¹F. S. Ham, *J. Phys. Chem. Solids* **6**, 335 (1958).
- ¹²J. Bailey and E. R. Weber, *Phys. Status Solidi A* **137**, 515 (1993).
- ¹³K. Sumino, *Phys. Status Solidi A* **171**, 111 (1999).
- ¹⁴T. Aoki, H. Kariyazaki, K. Sueoka, E. Toyoda, and K. Izunome, *Jpn. J. Appl. Phys.* **49**, 035501 (2010).
- ¹⁵J. Schön, H. Habenicht, M. C. Schubert, and W. Warta, *Solid State Phenom.* **156–158**, 223 (2010).
- ¹⁶M. Seibt, D. Abdelbarey, V. V. Kveder, C. Rudolf, P. Saring, L. Stolze, and O. Voß, *Mater. Sci. Eng., B* **159–160**, 264 (2009).
- ¹⁷R. Bullough and R. C. Newman, in *Progress in Semiconductors, Vol. 7*, edited by A. F. Gibbons and R. E. Burgess (Heywood, London, 1963), p. 100.
- ¹⁸A. Haarahiltunen, V. Vähänissi, M. Yli-Koski, H. Talvitie, and H. Savin, *Solid State Phenom.* **156–158**, 27 (2010).
- ¹⁹Synopsys Sentaurus Process User's Manual, Release: A-2010.03, Synopsys Inc., Zurich Switzerland, www.synopsys.com, (2010).
- ²⁰J. Schön and W. Warta, in *Proceedings of the 24th European Photovoltaic Solar Energy Conference* (WIP, Valencia, Spain, 2008), p. 1851–4.
- ²¹S. K. Estreicher, M. Sanati, and N. Gonzalez Szwacki, *Solid State Phenomena* **131–133**, 233–240 (2008).
- ²²D. Gilles, W. Schröter, and W. Bergholz, *Phys. Rev. B* **41**, 5770 (1990).
- ²³J. Schön, M. C. Schubert, W. Warta, H. Savin, and A. Haarahiltunen, *Phys. Status Solidi A* **207**, 2589 (2010).
- ²⁴D. Macdonald, J. Tan, and T. Trupke, *J. Appl. Phys.* **103**, 073710 (2008).
- ²⁵L. J. Geerligs and D. Macdonald, *Appl. Phys. Lett.* **85**, 5227 (2004).
- ²⁶M. C. Schubert, M. J. Kerler, and W. Warta, *J. Appl. Phys.* **105**, 114903 (2009).
- ²⁷A. A. Istratov, H. Hieslmair, and E. R. Weber, *Appl. Phys. A* **A69**, 13 (1999).
- ²⁸D. Macdonald, T. Roth, P. N. K. Deenapanray, T. Trupke, and R. A. Bardos, *Appl. Phys. Lett.* **89**, 142107 (2006).
- ²⁹S. Riepe, I. E. Reis, W. Kwapil, M. A. Falkenberg, J. Schön, H. Behnken, J. Bauer, D. Kreßner-Kiel, W. Seifert, and W. Koch, *Phys. Status Solidi C*, **8**, 733 (2010).
- ³⁰H. Habenicht, S. Riepe, O. Schultz, and W. Warta, in *Proceedings of the 24th European Photovoltaic Solar Energy Conference* (WIP, Milan, Italy, 2007), p. 1519–23.
- ³¹M. C. Schubert, W. Kwapil, J. Schoen, H. Habenicht, M. Kasemann, P. Gundel, M. Blazek, and W. Warta, *Sol. Energy Mater. Sol. Cells* **94**, 1451 (2010).
- ³²A. Bentzen, A. Holt, R. Kopecek, G. Stokkan, J. S. Christensen, and B. G. Svensson, *J. Appl. Phys.* **99**, 093509 (2006).
- ³³Y. C. Fan, J. Tan, S. P. Phang, and D. Macdonald, in *Proceedings of the 35th IEEE Photovoltaic Specialists Conference* (Hawaii, USA), p. 000439–42.
- ³⁴R. Kvande, L. J. Geerligs, G. Coletti, L. Arnberg, M. Di Sabatino, E. J. Øvrelid, and C. C. Swanson, *J. Appl. Phys.* **104**, 064905 (2008).
- ³⁵G. Coletti, R. Kvande, V. D. Mihailetschi, L. J. Geerligs, L. Arnberg, and E. J. Øvrelid, *J. Appl. Phys.* **104**, 104913 (2008).
- ³⁶M. Aoki and A. Hara, *J. Appl. Phys.* **74**, 1440 (1993).
- ³⁷C. Donolato, *Semicond. Sci. Technol.* **8**, 45 (1993).